S2S Prediction in GFDL SPEAR

MJO Diversity and Teleconnections

Baoqiang Xiang, Lucas Harris, Thomas L. Delworth, Bin Wang, Guosen Chen,
Jan-Huey Chen, Spencer K. Clark, William F. Cooke, Kun Gao, J. Jacob Huff,
Liwei Jia, Nathaniel C. Johnson, Sarah B. Kapnick, Feiyu Lu, Colleen McHugh,
Yongqiang Sun, Mingjing Tong, Xiaosong Yang, Fanrong Zeng, Ming Zhao,
Linjiong Zhou, and Xiaqiong Zhou

ABSTRACT: A subseasonal-to-seasonal (S2S) prediction system was recently developed using the GFDL Seamless System for Prediction and Earth System Research (SPEAR) global coupled model. Based on 20-yr hindcast results (2000–19), the boreal wintertime (November–April) Madden–Julian oscillation (MJO) prediction skill is revealed to reach 30 days measured before the anomaly correlation coefficient of the real-time multivariate (RMM) index drops to 0.5. However, when the MJO is partitioned into four distinct propagation patterns, the prediction range extends to 38, 31, and 31 days for the fast-propagating, slow-propagating, and jumping MJO patterns, respectively, but falls to 23 days for the standing MJO. A further improvement of MJO prediction requires attention to the standing MJO given its large gap with its potential predictability (15 days). The slow-propagating MJO detours southward when traversing the Maritime Continent (MC), and confronts the MC prediction barrier in the model, while the fast-propagating MJO moves across the central MC without this prediction barrier. The MJO diversity is modulated by stratospheric quasi-biennial oscillation (QBO): the standing (slow-propagating) MJO coincides with significant westerly (easterly) phases of QBO, partially explaining the contrasting MJO prediction skill between these two QBO phases. The SPEAR model shows its capability, beyond the propagation, in predicting their initiation for different types of MJO along with discrete precursory convection anomalies. The SPEAR model skillfully predicts the observed distinct teleconnections over the North Pacific and North America related to the standing, jumping, and fast-propagating MJO, but not the slow-propagating MJO. These findings highlight the complexities and challenges of incorporating MJO prediction into the operational prediction of meteorological variables.

KEYWORDS: Madden-Julian oscillation; Forecast verification/skill; Hindcasts; Model initialization; Subseasonal variability; Teleconnections

AFFILIATIONS: Xiang, J.-H. Chen, Cooke, Huff, and Jia—NOAA/Geophysical Fluid Dynamics Laboratory, Princeton, New Jersey, and University Corporation for Atmospheric Research, Boulder, Colorado; **Harris, Delworth, Johnson, Kapnick, Tong, Yang, Zeng, and Zhao**—NOAA/Geophysical Fluid Dynamics Laboratory, Princeton, New Jersey; **Wang**—International Pacific Research Center, University of Hawai'i at Mānoa, Honolulu, Hawaii; **G. Chen**—Earth System Modeling Center, Key Laboratory of Meteorological Disaster of Ministry of Education, Collaborative Innovation Center on Forecast and Evaluation of Meteorological Disasters, Nanjing University of Information Science and Technology, Nanjing, China; **Clark**—NOAA/Geophysical Fluid Dynamics Laboratory, Princeton, New Jersey, and Vulcan Inc., Seattle, Washington; **Gao, Lu, Sun, and L. Zhou**—NOAA/Geophysical Fluid Dynamics Laboratory, and Cooperative Institute for Modeling the Earth System, Program in Oceanic and Atmospheric Sciences, Princeton, New Jersey; **McHugh**—NOAA/Geophysical Fluid Dynamics Laboratory, Princeton, New Jersey, and Science Applications International Corporation, Reston, Virginia; **X. Zhou**—University Corporation for Atmospheric Research, Boulder, Colorado, and Environmental Modeling Center, NOAA/NWS/NCEP, College Park, Maryland

A pioneering work by Xie et al. (1963) revealed a local oscillatory signal with a prominent 40–50-day period in the western Pacific that has strong modulation on tropical cyclone activities (also see Li et al. 2018). Madden and Julian (1971, 1972) discovered a global-scale 40–50-day oscillatory mode with pronounced eastward propagation across the whole tropics, known as the Madden–Julian oscillation (MJO). The development and evolution of MJO involve interactions of convection, planetary boundary layer, wave dynamics, moisture, and radiation, and it is also significantly modified by multiscale interaction and air–sea coupling. Given the complexity of MJO, many theories have been proposed to explain the essential processes responsible for its existence, scale selection, and propagation (e.g., Jiang et al. 2020; Zhang et al. 2020).

Compared to synoptic weather variability, the MJO has longer persistence and an oscillatory nature, highlighting the importance of MJO prediction for subseasonal-to-seasonal (S2S) predictions of climate and extreme weather events. For example, the prediction of MJO has been demonstrated to be critical for the medium-range to the subseasonal prediction of tropical cyclones (Jiang et al. 2018; Lee et al. 2018, 2020; Vitart 2009; Xiang et al. 2015a). A skillful MJO prediction also benefits the prediction of phenomena including the North Atlantic Oscillation (Lin et al. 2010), atmospheric rivers (DeFlorio et al. 2018; Mundhenk et al. 2018), and the U.S. precipitation (Nardi et al. 2020).

Dynamical models have become the primary tool for MJO prediction. Extensive exploration of the predictability of the MJO in dynamical models has achieved substantial advances in recent decades, while a big gap still remains between the prediction skill and the potential predictability (Kim et al. 2018, 2019; Neena et al. 2014; Vitart 2017). A myriad of factors influence MJO prediction, each different among models, such as the convection parameterization (Zhu et al. 2020), air–sea coupling (Fu et al. 2013; Harris et al. 2020; Zhu and Kumar 2019), and initialization (Ren et al. 2016; Wu et al. 2020). Additionally, the stratospheric quasi-biennial oscillation (QBO) can rectify the MJO activities (MJO days) and propagation, and influence its prediction skill (Lim et al. 2019; Marshall et al. 2017; Martin et al. 2021; S. Wang et al. 2019; Zhang and Zhang 2018). Some systematic biases in model mean states and feedback processes are shown to exert direct effects on the MJO prediction skill (Kim et al. 2019; Lim et al. 2018).

It is worth noting that individual MJO events vary markedly from event to event in their amplitude, life cycle, and propagation (Wang and Rui 1990). Kim et al. (2014) revealed that

some MJO events propagate across the Maritime Continent (MC) while some others do not. Actually, about 40% of the observed MJO events are blocked by the MC (Kerns and Chen 2020). On the basis of the substantially different propagation features of individual MJO events, B. Wang et al. (2019) separated the MJO events into four clusters using a clustering method (standing, jumping, slow-propagating, and fast-propagating events). The standing MJO is referring to the events with a locally oscillatory feature in the Indian Ocean without evident propagation. The jumping MJO represents the cases with a sudden migration of anomalous convection from the eastern Indian Ocean to the western Pacific. They claimed that their existence is controlled by different large-scale background mean states and interaction between tropical wave dynamics and convection. It prompts the question of whether the MJO prediction depends on the MJO propagation characteristic? The objective of this study is twofold: first, to introduce a recently developed prediction modeling system targeting S2S prediction, and second, to identify the potential skill dependence on MJO diversity using this prediction system.

The paper is organized as follows. The next section introduces the model, experiments, and methodology. The following sections describe the overall MJO prediction skill and the skill dependence on MJO diversity, respectively. Then, the model prediction of MJO propagation, initial development, and teleconnections in the context of MJO diversity are presented. The paper concludes with a summary and discussion.

Model, hindcast experiments, and methodology

Model and hindcast experiments. We use the Geophysical Fluid Dynamics Laboratory (GFDL) Seamless System for Prediction and Earth System Research (SPEAR) coupled model. The model was developed as the next generation GFDL modeling system for seasonal to multidecadal prediction and projection (Bushuk et al. 2021; Delworth et al. 2020; Lu et al. 2020; Murakami et al. 2020). To approach the seamless suite of prediction, here, we extend the research focus to the S2S time scale. The SPEAR model shares many components with the GFDL CM4.0 model (Held et al. 2019). In particular, SPEAR uses an atmospheric and land model identical to AM4.0/LM4.0 (Zhao et al. 2018a,b) but with a dynamical vegetation model and a lower-resolution MOM6 (Adcroft et al. 2019). There are three configurations of SPEAR that share the same ocean model (horizontal resolution of about 1° and 75 vertical levels) but with three different atmospheric horizontal resolutions, which are referred to as SPEAR_LO (1°), SPEAR_MED (0.5°), and SPEAR_HI (0.25°). SPEAR_MED uses a 0.5° AM4.0, which contains 33 vertical levels with the top of the atmosphere at 1 hPa (Zhao 2020). SPEAR_MED has been demonstrated to produce realistic simulations of extreme weather statistics such as the frequency of tropical cyclones (Murakami et al. 2020), atmospheric rivers (Zhao 2020), and mesoscale convective systems (Dong et al. 2021). SPEAR_MED is used in this study for S2S prediction, and we refer to it as SPEAR hereinafter for simplicity. This model has shown a realistic MJO simulation from its control run (Delworth et al. 2020), offering an excellent opportunity to study the MJO prediction and some related issues. The reader is referred to Delworth et al. (2020) for additional details about this model.

Similar to Xiang et al. (2015b), initial conditions for the atmosphere and ocean were generated through a simple nudging technique toward observations with several years' integration before prediction. The atmospheric nudging fields include winds, temperature, and specific humidity using the Modern-Era Retrospective Analysis for Research and Applications, version 2 (MERRA-2), analysis data (6-hourly interval) (Gelaro et al. 2017). The sea surface temperature (SST) is nudged to NOAA Optimum Interpolation 1/4° Daily SST Analysis (OISST v2) (Reynolds et al. 2007). Using the same SPEAR model, the ocean initialization for S2S prediction is much simpler than the seasonal-to-decadal prediction system that adopts a comprehensive ocean data assimilation system (Lu et al. 2020), allowing a later assessment of the potential

roles of subsurface ocean initialization on S2S prediction. Hindcasts were carried out every 5 days from January 2000 to April 2019, and 10 ensemble members were generated by using perturbed nudging strengths for both the atmosphere and the ocean SST so that they differ from one another in the initial conditions. The nudging of circulation is applied to the whole atmosphere. However, the nudging of moisture field is confined in the free atmosphere with the lowest several model layers (roughly the boundary layer) unperturbed, considering the fact that the moisture field in analysis data are relatively less reliable than other variables and the nudging of moisture within boundary layer may induce large initial shock in a coupled system via strongly altering latent heat flux. Since the MJO is most pronounced in boreal wintertime, we focus on the period from November to the ensuing April. We made 708 hindcast events, and each has 10 members. We integrated each hindcast for 45 days.

Methodology. The observational anomalies were obtained by removing the time mean and the first three harmonics of the observational climatological annual cycle and subtracting the time-mean anomalies over the previous 120 days. The hindcast anomalies are calculated by removing the model hindcast climatology and also the previous 120 days' time-mean anomalies.

The evaluation procedure for MJO prediction is similar to Xiang et al. (2015b) and adopts the widely used real-time multivariate MJO (RMM) index (Wheeler and Hendon 2004) as a metric to measure the MJO and its prediction. The anomalies of outgoing longwave radiation (OLR) and 850- and 200-hPa zonal winds are then projected onto two observed leading multivariate empirical orthogonal function (EOF) modes to obtain the RMM indices (Wheeler and Hendon 2004) (Fig. ES1 in the online supplemental material). The first (second) mode represents the phases with anomalous convection in the Indian Ocean (western Pacific). The observed and predicted two RMM indices (RMM1 and RMM2) are then normalized by the standard deviation of the observed RMM indices. Using the above RMM indices as the predictands, the so-called bivariate anomaly correlation coefficient (ACC) and root-mean-square error (RMSE) were used here to measure its forecast skill following Lin et al. (2008). The MJO amplitude is defined as $\sqrt{RMM1^2 + RMM2^2}$.

For verification, the data we used comprise the NOAA daily mean interpolated OLR data (Liebmann and Smith 1996) and ERA-5 reanalysis data as observations (C3S 2017), including winds, 2-m air temperature (t2m), geopotential height, and specific humidity. All data are interpolated to $1° \times 1°$ resolution for analysis.

Overall evaluation of the MJO prediction

Figure 1a shows the bivariate ACC of MJO prediction in boreal wintertime (November–April) evaluated based on all the hindcasts (708 cases with 10 ensemble members). The mean skill from a single member is about 23 days, as determined by the maximum lead time with the ACC exceeding 0.5. As expected, the ACC for the 10-member ensemble-mean is superior to individual members, with a prediction skill of 30 days. The prediction skill is nearly saturated when using five ensemble members (29 days), and additional ensemble members add little to the MJO prediction skill (Fig. ES2). The ensemble spread is much smaller than the RMSE (Fig. 1b), indicating an underdispersive ensemble that may limit the overall prediction skill of this system. The 10-member ensemble mean serves as the basis for all the following analyses, except where otherwise noted.

We further investigate the skill dependence on the MJO initial and target amplitude and phases. The skill has a much smaller difference between the initially strong (|RMM| > 1) and weak (|RMM| < 1) cases than the target strong and weak cases (Fig. 2a vs Fig. 2c). Here, the target cases are referring to the MJO events during the forecast period. In other words, the skill is more sensitive to the target MJO amplitude during the forecast period than its initial

amplitude. Note that some models experience strong sensitivity with initial amplitude, but some do not (Lim et al. 2018). The skill also differs among different MJO phases. A relatively higher skill is found when initiated at phases 3 and 4 with the anomalous wet phase in the eastern Indian Ocean and MC. In comparison, the skill is relatively lower during phases 1 and 2 when the anomalous intense convection occurs in the western and central Indian Ocean (Fig. 2b). The skill is higher for the target phases 3 and 4 than the target phases 5 and 6 (Fig. 2d). The above skill dependence on MJO amplitude and phase is generally similar to a previous version of the GFDL model (Xiang et al. 2015b).

The MJO prediction skill is determined by the error growth in amplitude and propagation speed. Here we examine the MJO amplitude and its phase angle error for initially strong MJO cases (Fig. 3). The phase angle error is estimated between the observed and predicted RMM index following Rashid et al. (2011). The predicted MJO amplitude agrees well with observation during the first 10 days but then decreases very rapidly (Fig. 3a) along with the increase of noise. During the first 25 days, the predicted mean amplitude is comparable but slightly weaker (by 7.7%) than observations. The mean phase angle error in the first 25 days is −4.0° (Fig. 3c), with a magnitude generally smaller than 10.0° for individual phases (Fig. 3d). The individual member has a similar amplitude as observations (Fig. 3a), implying that the amplitude error from ensemble mean is largely attributed to the rapid increase of noise. Compared with a previous version of the GFDL model (Xiang et al. 2015b), the predicted amplitude error (phase angle error) in the first 25 days is reduced by 38% (5%), in agreement with an overall improved MJO prediction skill (30 vs 27 days).
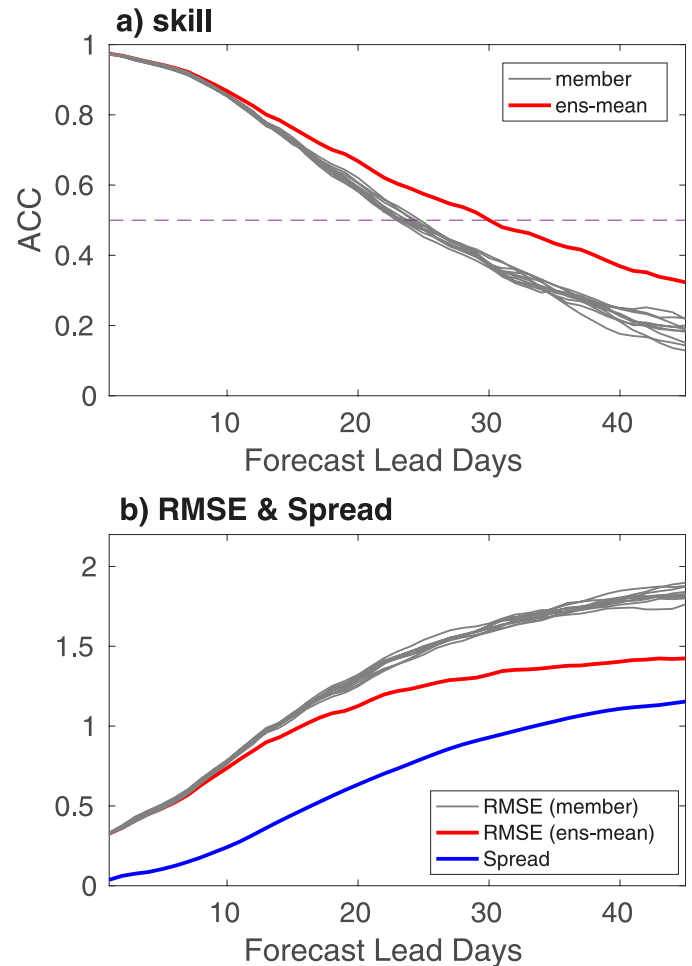

Fig. 1. MJO prediction skill during boreal wintertime (November–April) from 2000 to 2019 made by the GFDL SPEAR model. (a) The bivariate anomalous correlation coefficient (ACC) measured by the RMM index from individual members (gray) and 10-member ensemble mean (red). (b) The RMM index root-mean-square error (RMSE) from individual members (gray) and their ensemble mean (red). The blue line denotes the ensemble spread relative to the 10-member ensemble mean.
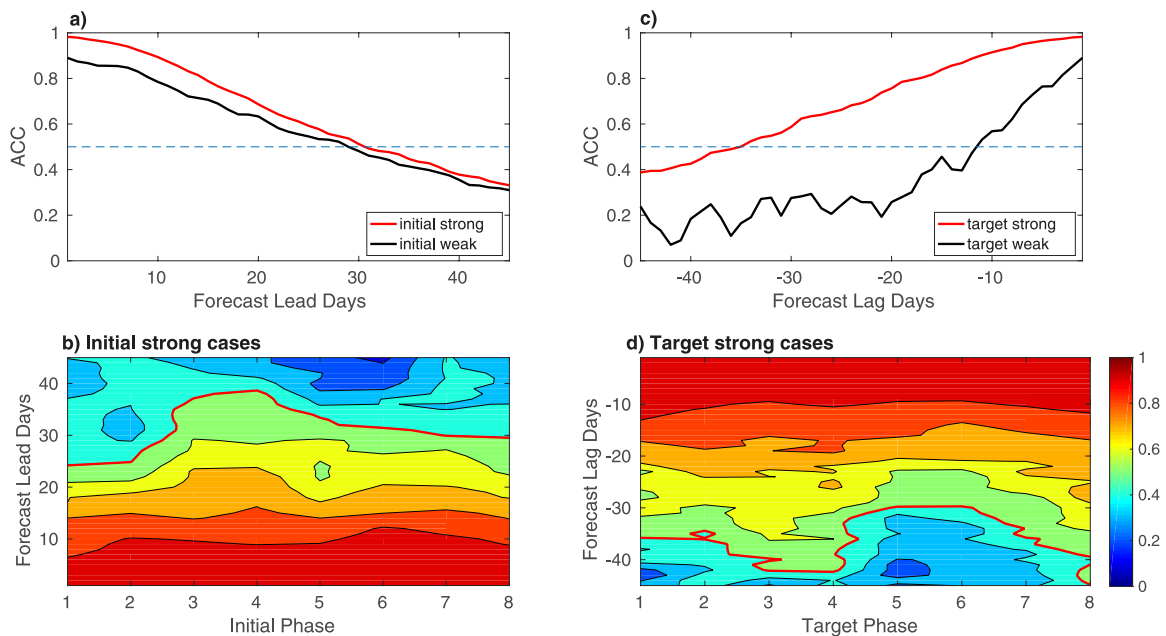
Skill dependence on MJO diversity

Given the contrasting propagation behaviors for individual MJO events, it is natural to question whether the MJO prediction is dependent on its propagation patterns. The first step to address this question is to identify individual MJO events. Following B. Wang et al. (2019), an MJO event is selected when the area-averaged OLR anomalies in the equatorial Indian Ocean (75°–95°E, 10°S–10°N) are negative and have an amplitude greater than one standard deviation for 5 successive days (roughly during the MJO phases 2 and 3). A K-means cluster analysis (Kaufman and Rousseeuw 2009) is then applied to classify the MJO events based on their propagation patterns. This analysis identifies four types of MJO events: standing, jumping, slow-propagating, and fast-propagating types (B. Wang et al. 2019). Eventually, 55 MJO events were identified during the studied period from January 2000 to April

Fig. 2. (a) The bivariate ACC for initially strong (red) and initially weak (black) MJO cases. **(b)** The ACC as a function of initial phases (*x* axis) and forecast lead days (*y* axis). **(c)** The bivariate ACC for target strong (red) and target weak (black) MJO cases as a function of forecast lag days. **(d)** The ACC as a function of target phases and forecast lag days. "Strong MJO" (weak MJO) is defined as all days with |RMM| > 1 (|RMM| < 1).

2019, including 12 standing, 14 jumping, 15 slow-propagating, and 13 fast-propagating cases (Table 1). Their contrasting propagation features are apparent from the composite OLR anomalies centered in the midpoint of the selected events (day 0) (Figs. 4c–f).
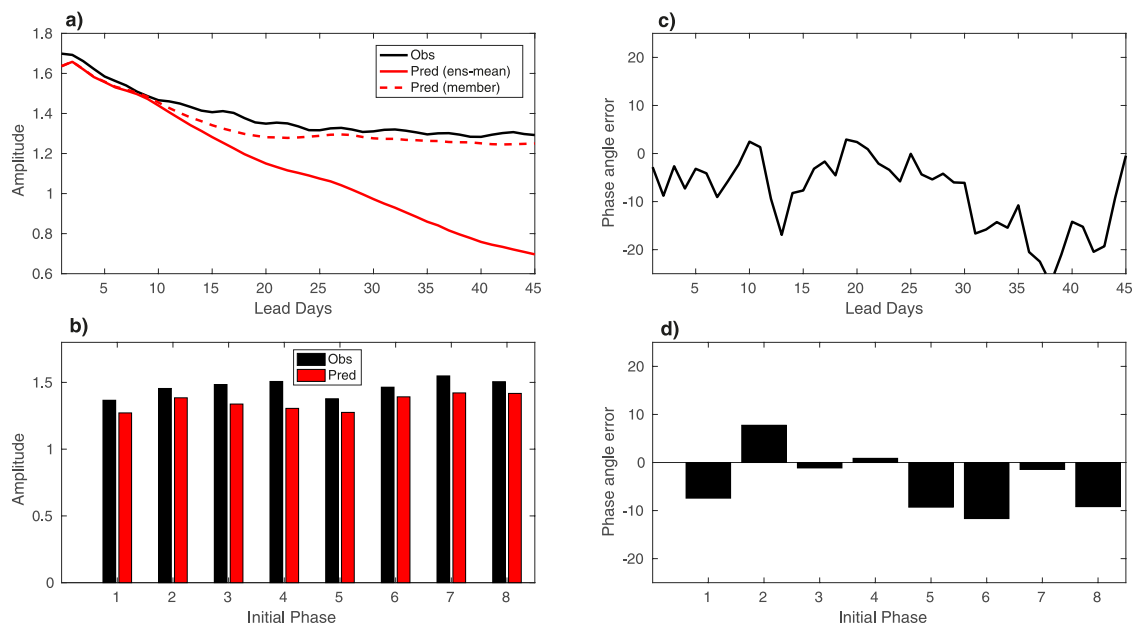

Fig. 3. Prediction of MJO amplitude and phase angle. (a) The time evolution of MJO amplitude as a function of forecast lead days for initially strong cases from observations (black) and model prediction from the ensemble mean (solid red) and mean of individual members (dashed red). **(b)** The observed (black bars) and predicted (red bars) MJO amplitude averaged over the first 25 days for initially strong cases as a function of eight different MJO phases (*x* axis). **(c)** Prediction of MJO phase angle error (°) as a function of forecast lead time for the initially strong cases. **(d)** The predicted MJO phase error averaged over the first 25 days for initially strong cases as a function of eight different MJO phases (*x* axis).

Table 1. The temporal midpoint of the selected four clusters of the observed MJO events. Each MJO case is defined when the area-averaged OLR anomalies in the equatorial Indian Ocean (75°–95°E, 10°S–10°N) are below one standard deviation for 5 successive days. The total number of events is shown in the first row in the parentheses.

Standing (12)	Jumping (14)	Slow propagating (15)	Fast propagating (13)
31 Jan 2003	22 Jan 2002	18 Nov 2000	30 Apr 2002
9 Nov 2003	21 Mar 2002	27 Jan 2001	13 Nov 2002
18 Feb 2005	1 Nov 2004	18 Nov 2001	9 Dec 2003
16 Nov 2008	4 Jan 2005	23 Dec 2002	29 Mar 2005
25 Nov 2010	12 Dec 2005	11 Jan 2006	25 Dec 2006
3 Feb 2011	23 Apr 2006	19 Mar 2006	9 Apr 2009
27 Nov 2011	27 Mar 2010	13 Dec 2007	9 Mar 2012
21 Dec 2011	30 Apr 2011	28 Jan 2008	5 Nov 2012
21 Apr 2012	27 Jan 2012	10 Nov 2009	27 Dec 2012
1 Jan 2017	6 Feb 2016	30 Dec 2009	18 Apr 2018
26 Feb 2017	15 Mar 2016	12 Feb 2010	19 Jan 2019
12 Apr 2017	28 Nov 2017	8 Feb 2013	3 Mar 2019
	20 Jan 2018	31 Mar 2013	23 Apr 2019
	5 Mar 2018	11 Feb 2015	
		5 Apr 2015	

For each MJO cluster, we consider all the hindcasts initiated during the period between 20 days before and 15 days after the midpoint of the selected event (day 0), approximately covering the life cycle of the selected cases. Since the hindcasts are carried out every 5 days, the total forecast case numbers are 88, 104, 116, and 92 for the standing, jumping, slow-propagating, and fast-propagating MJO, respectively. Results show that the fast-propagating MJO possesses the best prediction skill of 38 days (Fig. 4a). The jumping MJO attains a similar prediction skill with the slow-propagating MJO (31 days), albeit the jumping MJO is categorized into the nonpropagating group (B. Wang et al. 2019). The standing MJO has the lowest skill (23 days). We conclude that the model tends to be more skillful in predicting the propagating and jumping MJO than the standing MJO.

The distinct MJO prediction skill among four clusters of MJO is possibly related to their potential predictability. Based on the perfect model assumption, the potential predictability can be estimated by taking one ensemble member as the truth and the ensemble mean of the other members as predictions. The four clusters of MJO exhibit similar potential predictability (38–39 days) (Fig. 4b), which obviously cannot explain the contrasting prediction skill as shown in Fig. 4a. We also infer that there is much larger room to improve the prediction of the standing MJO than the other types of MJO, and a further MJO skill enhancement in SPEAR primarily relies on advancing the standing MJO prediction.

More insights into the skill dependence on MJO types can be gained by examining the relationship between the MJO prediction and its amplitude (Fig. 5a). For the standing (fast-propagating) MJO, the initially weak cases have relatively lower (higher) skills than the initially strong cases. However, for both the jumping and slow-propagating MJO the model shows a comparable skill between the initially weak and strong cases. The skill spread among different groups of MJO tends to be larger for the initially weak cases than the initially strong cases. Intriguingly, a very similar skill is found for these four types of MJO when initiated at very strong MJO ($|RMM| > 1.5$) (not shown). The MJO prediction is less sensitive to the target amplitude. The skill for target strong (weak) cases is around 35 (10) days for all four clusters of MJO (Fig. ES3). Therefore, the overall skill diversity (Fig. 4a) is primarily related to the skill difference for initially weak cases.
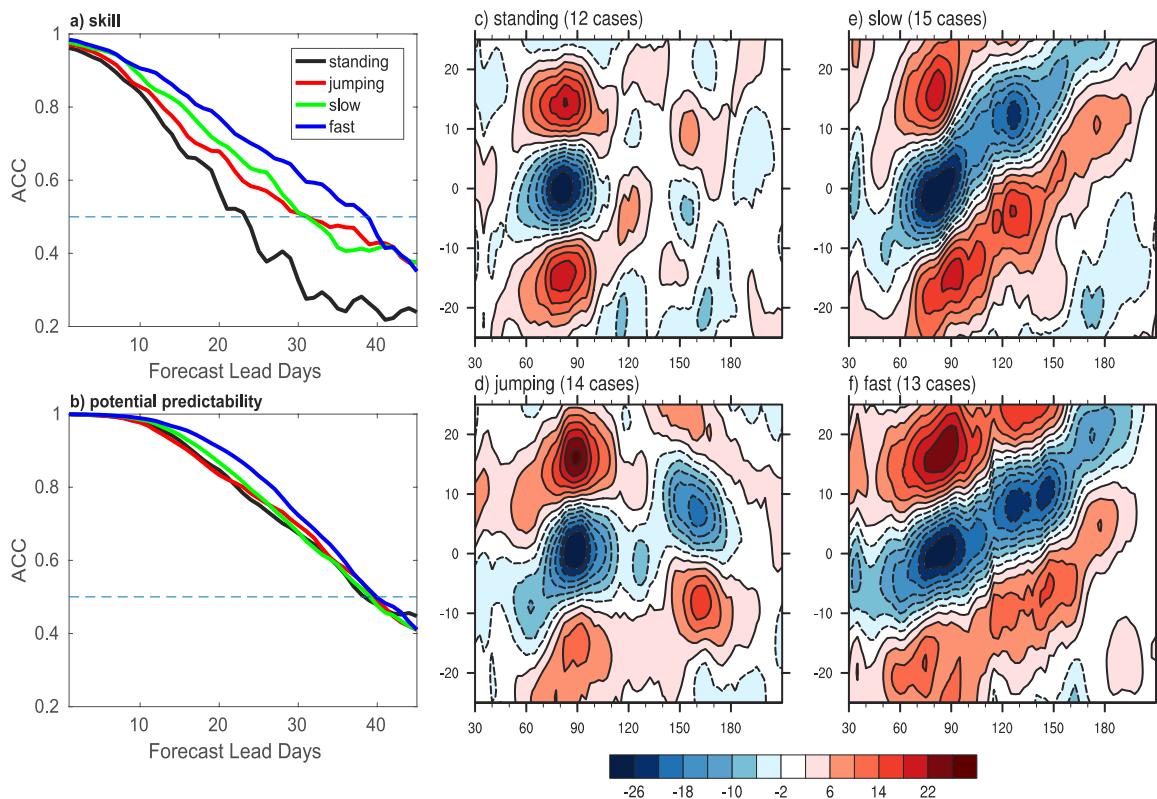
Fig. 4. Four types of MJO events and their prediction skills in the SPEAR model. (a) The ACC and (b) potential predictability for four clusters of MJO. (c)–(f) Longitude (*x* axis)–time (*y* axis) composite of equatorial (10°S–10°N) OLR anomalies (W m⁻²) for four types of MJO centered at day 0 when the domain-averaged OLR anomalies in the equatorial Indian Ocean (75°–95°E, 10°S–10°N) are below one standard deviation for 5 successive days.

The observed MJO amplitude differs substantially among different types of MJO. Figure 5b displays the observational MJO amplitude for individual groups during the whole forecast period (45 days) by counting all the selected cases. The fast-propagating MJO has the strongest amplitude, followed by the slow-propagating, the jumping MJO, and the standing MJO, which has the smallest mean MJO amplitude. Given this, there are more weak cases for the standing MJO than the other groups, which may account for the overall lower skill for the standing MJO considering the skill dependence on the amplitude. Compared to the fast-propagating MJO, the relatively lower skill for the slow-propagating MJO may reflect the MC prediction barrier effects (Kim et al. 2018; Weaver et al. 2011), and we will discuss this later.

One may wonder whether the relatively lower prediction skill for the standing MJO is related to the intrinsic limitation of the metrics used (bivariate ACC of RMM indices) that may not be appropriate to represent its standing feature in the Indian Ocean (Fig. 4c). To address this, we examine the prediction skill of convection and circulation anomalies in the equatorial Indian Ocean (Fig. ES4). The skill difference among the four MJO types is broadly consistent with that based on the bivariate ACC (Fig. ES4 vs Fig. 4a), confirming the robustness of the results.

Prediction of MJO propagation diversity and its interannual modulations
Prediction of the diverse MJO propagations and the underlying mechanisms. Figure 6 compares the observed and predicted equatorial (10°S–10°N) propagation features of MJO initiated 5 days before the peak phase in the equatorial Indian Ocean (day −5). The broad features of the observed standing, jumping, and slow- and fast-propagating MJO events (top two rows) are predicted reasonably well when initiated at day −5 (bottom two rows) despite an underpredicted amplitude. One noticeable deficiency is the underpredicted propagation

speed for the slow-propagating MJO initiated at day −5. The predicted convective anomalies gradually fade when reaching the MC without further propagation to the western Pacific (Fig. 6). For the slow-propagating MJO, the issue of underpredicted convection anomalies tends to be more severe when initiated at day −10, together with a too slow propagation (Fig. ES5). This is partially responsible for the lower prediction skill than the fast-propagating MJO.

Extensive studies have been conducted to study the mechanisms for MJO propagations. One group accentuates the role of preconditioning characterized by lower-tropospheric moistening ahead of major convection (Benedict and Randall 2007; Hsu and Li 2012; Kiladis et al. 2005; Wang and Lee 2017). Figure 6 shows that for the standing and jumping MJO, the lower-tropospheric convergence and moistening are in phase with the convective anomalies in the Indian Ocean, cohesive with their rather stationary feature in the Indian Ocean. For the jumping MJO, the anomalous convergence and moistening in the MC even slightly lead the major convection in the Indian Ocean, providing a pathway for the fast transition of convection from the Indian Ocean to the western Pacific. For both the slow and fast-propagating MJO, there is an evident premoistening characterized by lower-tropospheric convergence and moistening located to the east of the major deep convection. The model prediction qualitatively agrees with observations, while the low-tropospheric convergence almost disappears to the east of 150°E for all groups of MJO suggestive of a systematic model bias.

Fig. 5. Prediction skill dependence of MJO diversity on the initial amplitude. (a) The ACC for four types of MJO initiated at strong (|RMM| > 1; solid) and weak (|RMM| < 1; dash) cases. (b) The observed MJO amplitude $\sqrt{RMM1^2 + RMM2^2}$ for four groups of MJO as a function of forecast lead days (x axis) by counting all the selected cases (initiated between 20 days before and 15 days after day 0). There are 42, 59, 85, and 67 initially strong cases and 46, 45, 31, and 25 initially weak cases for the standing, jumping, slow-propagating, and fast-propagating MJO, respectively.

The premoistening is predominantly driven by the lower-tropospheric moisture convergence that is related to the Kelvin wave and the resultant equatorial low pressure at the top of the boundary layer (Haertel 2021; Hsu and Li 2012; Wang 1988; Wang and Lee 2017). Note that the convergence anomalies are mainly ascribable to zonal winds rather than meridional winds. We present, in Fig. 7, the spatial patterns of OLR, 850-hPa winds, and 850-hPa geopotential height anomalies. The model prediction initiated at day −5 generally resembles the observed characteristics for these four groups of MJO (Fig. 7).

Some indigenous features are identified among these four groups from observations (Fig. 7). The easterly wind anomalies over the MC and western Pacific are much weaker for the standing MJO than the other three groups. Given the strong zonal gradient of climatological moisture in the Indian Ocean, the westerly wind anomalies as a Rossby wave response induce a negative moisture advection and deteriorate the convection anomalies (Adames and Kim 2016), facilitating its phase transition. Meanwhile, the increased atmospheric stability due to convective
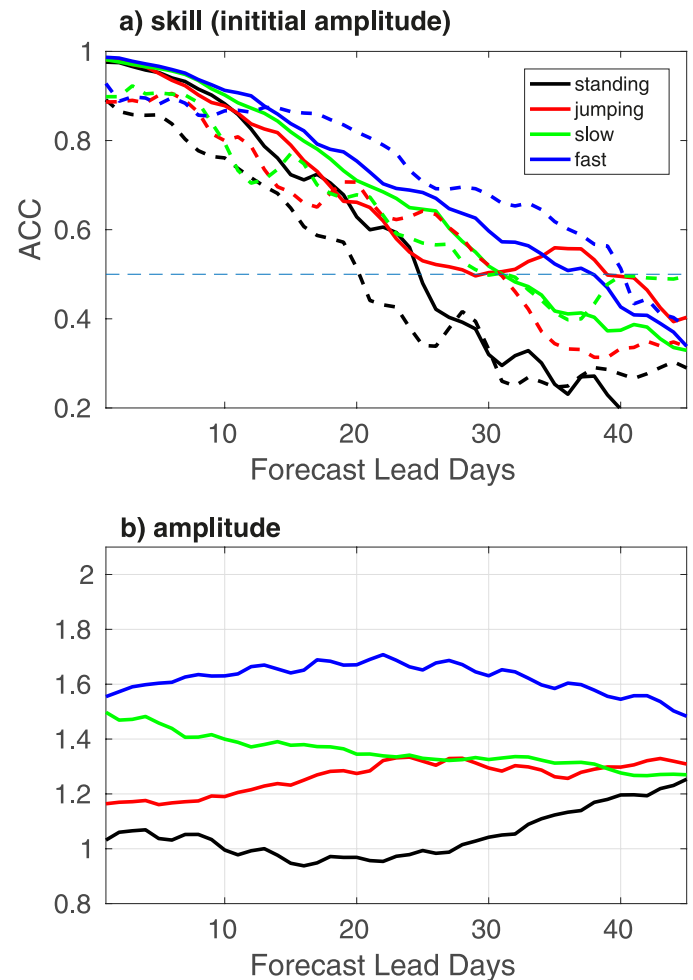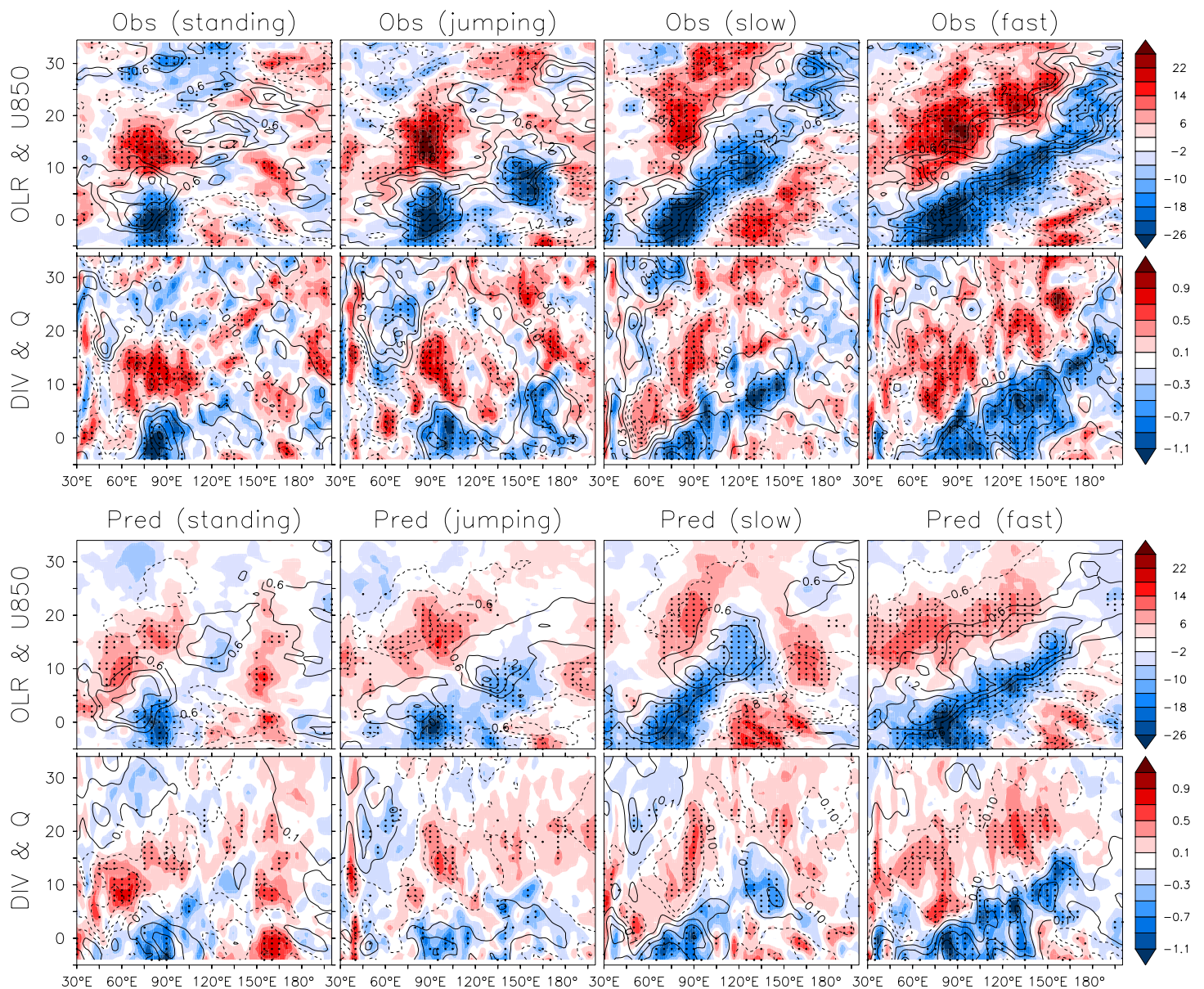
Fig. 6. MJO propagation and proposed mechanisms seen from the equatorial (10°S–10°N) anomalies as a function of longitude (*x* axis) and time lag (*y* axis; days) composited for four types of MJO. The first row shows observed OLR anomalies (shading; W m⁻²) and 850-hPa zonal winds (contours with an interval of 0.6 m s⁻¹). The second row depicts observed lower-tropospheric divergence (shading; 10⁻⁶ S⁻¹) averaged over two levels (850 and 925 hPa) and specific humidity (contours with an interval of 0.2 g kg⁻¹) averaged over two levels (700 and 825 hPa). The bottom two rows are similar to the top two but for model predictions initiated at day −5 (5 days before the peak phase in the Indian Ocean). The black stippling denotes the regions at the 10% significance level for OLR and lower-tropospheric divergence anomalies.

heating and the resultant decreased SST also contribute to its phase transition. The above physical processes represent a discharge–recharge process responsible for its local oscillatory feature (Bladé and Hartmann 1993). The jumping MJO possesses a weak Rossby wave response but with a far-reaching Kelvin wave component. Unlike the propagating MJO, the jumping MJO's easterly anomalies are confined in the western Pacific without penetrating the MC. The newly formed convection anomalies in the western Pacific are relatively independent of the preceding major convection in the Indian Ocean (Fig. 7). Another notable difference is that the drying anomalies in the MC and western Pacific are significantly weaker for both the standing and jumping MJO than the propagating MJO, which may have some consequences on the MJO propagation (Kim et al. 2014). For the fast-propagating MJO, the major convection is coupled to the strong Kelvin waves during the whole period when traversing the MC
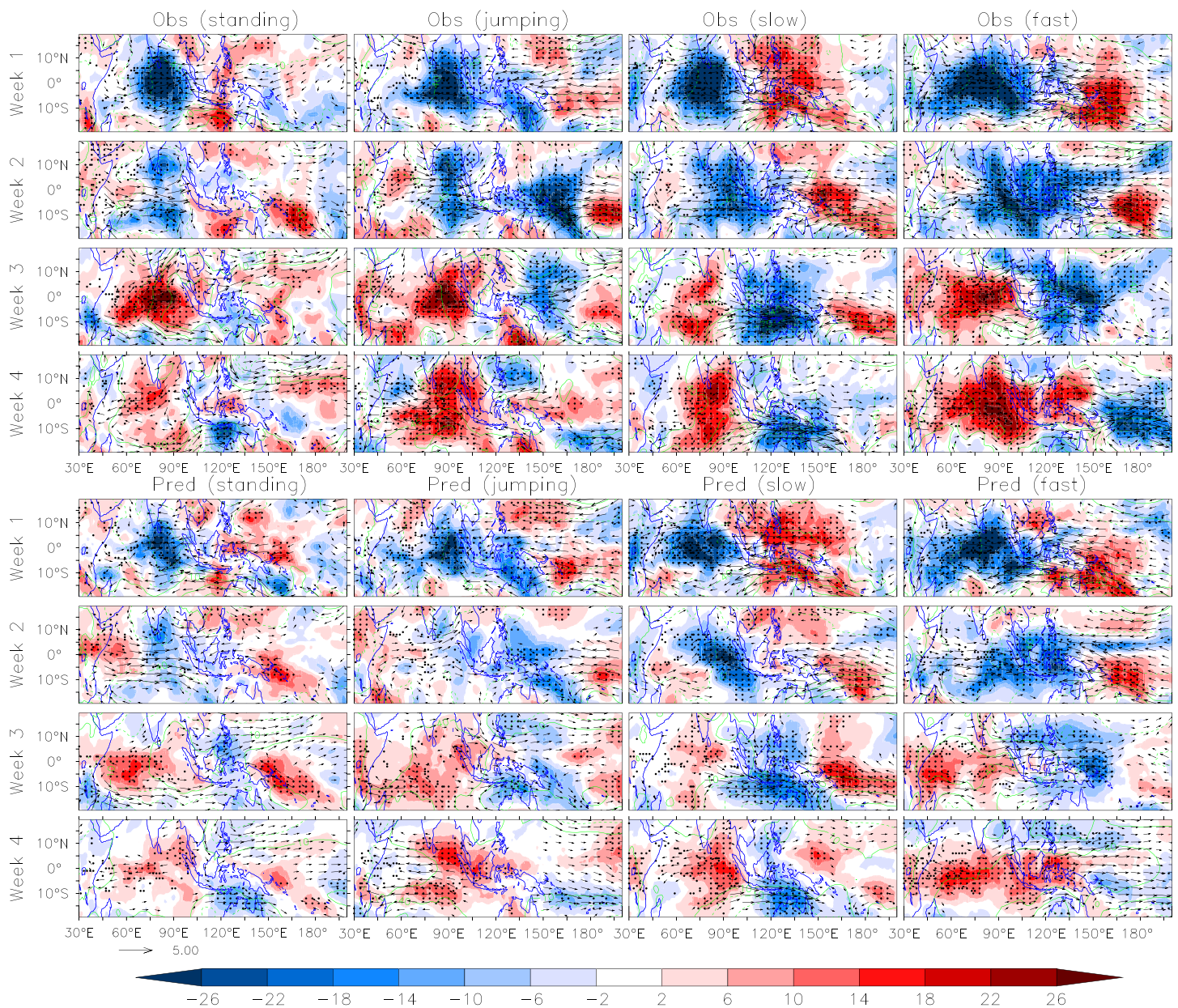
Fig. 7. Comparison of observed and predicted anomalies during the first 4 weeks initiated at day −5. The observed composite anomalies of OLR (W m^{-2}), 850-hPa winds (m s^{-1}; not shown when wind speed is less than 0.5 m s^{-1}), and 850-hPa geopotential height (contours; m^2 s^{-2}) during the (first row) first, (second row) second, (third row) third, and (fourth row) fourth weeks starting from day −5. The bottom four rows are similar to the top four but for model predictions initiated at day −5. The MJO type is indicated at the top of each column. The black stippling denotes the regions at the 10% significance level for OLR anomalies.

(Fig. 7). It has a rather meridionally symmetric pattern of anomalous convection during the first week. The major convection even migrates to the Northern Hemisphere together with a northwest–southeast-tilted structure at weeks 2 and 3.

The observed and predicted features for different kinds of MJO suggest that the tropical wave dynamics and its interaction with the lower-tropospheric moisture may play an important role in MJO propagation, a point emphasized by the so-called convection–dynamics–moisture trio-interaction theory (Wang et al. 2016). However, it is also noticed that for the slow-propagating MJO, the anomalous moisture anomalies tend to decouple from the Kelvin wave during week 3, accompanied by southeastward detouring convection–circulation anomalies to the south of MC. We argue that some other processes may contribute to its further eastward propagation from observations for the slow-propagating MJO, such as

the horizontal advection (Kim et al. 2017) or wind-induced surface heat exchange (WISHE) given the mean westerly winds in this region. However, the model presumably has difficulty capturing these possible processes, leading to the rapid termination of MJO in the eastern MC (Figs. 6 and 7). It is concluded that the slow-propagating MJO suffers the MC prediction barrier ~~from model predictions~~, while the fast-propagating MJO seemingly does not have this problem. The fast-propagating MJO has a larger zonal scale than the slow-propagating event, contributing to its faster propagation speed (Adames and Kim 2016; Chen and Wang 2020).

Observed and predicted impacts of ENSO and QBO on MJO diversity. What are the root causes for the diversified propagation for different types of MJO? Why are the equatorial waves so different for different types of MJO? One possibility is due to the regulation of interannual variability (Fig. 8). Here interannual variability is approximately estimated as the difference between the averaged 30-day unfiltered anomalies and the averaged 30-day anomalies with the previous 120-day anomalies removed. B. Wang et al. (2019) found that the standing (fast-propagating) MJO is related to a La Niña (central Pacific El Niño) background mean state, while no statistically significant SST anomalies are found in the equatorial Pacific. The results are overall consistent with B. Wang et al. (2019) but we also notice there is a significant
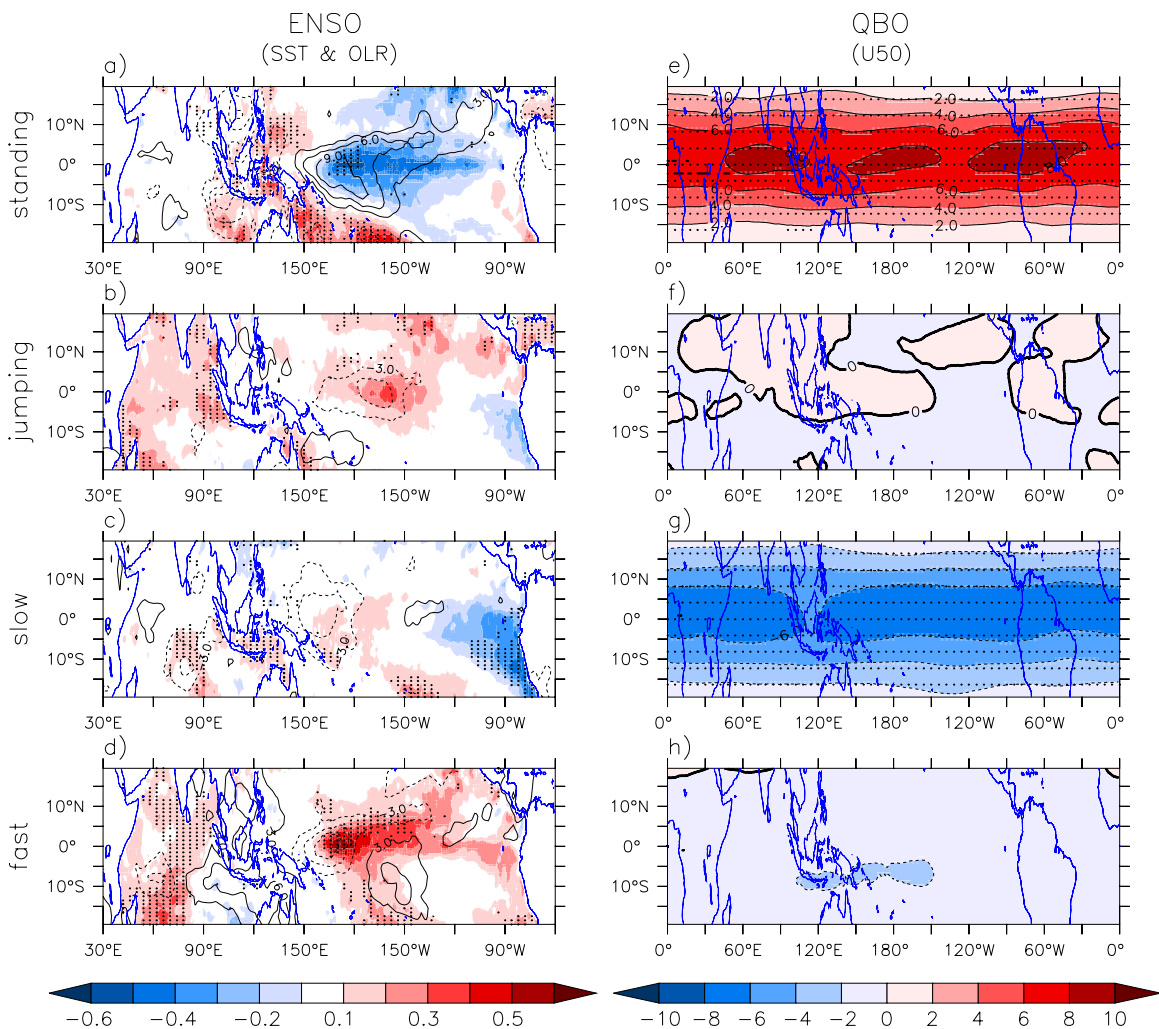

Fig. 8. Regulation of ENSO and stratospheric QBO on MJO diversity. (a)–(d) The observed interannual SST (°C; shading) and OLR anomalies (W m⁻²; contours) between day −15 and day +15. (e)–(h) The observed interannual 50-hPa zonal wind anomalies (m s⁻¹) between day −15 and day +15. The MJO type is indicated at the left of each row. The black stippling denotes the regions at the 10% significance level for SST anomalies in (a)–(d) and 50-hPa zonal wind anomalies in (e)–(h). Note that all cases initialized from November to April are used here.

SST cooling in the far eastern Pacific for the slow-propagating MJO (Fig. 8c), a signature of an increased zonal SST gradient similar to that for the fast-propagating MJO (Fig. 8d). The convection anomalies are dynamically coherent with the lower-boundary SST changes for different clusters of MJO. The modulation of El Niño–Southern Oscillation (ENSO) on MJO is arguably through two processes: the resultant expansion/shrinkage of the warm pool area that may alter the spatial scale of MJO (Lyu et al. 2021; B. Wang et al. 2019), and the change of mean moisture and vertical shear over the MC (Liu et al. 2020; Wei and Ren 2019).

Besides ENSO, the role of stratospheric QBO on the MJO activities (MJO frequency, duration, amplitude, and propagation) has been articulated recently given the tight QBO–MJO connection in boreal wintertime (Liu et al. 2014; Yoo and Son 2016; Zhang and Zhang 2018). The QBO–MJO coupling becomes even more prominent in recent decades (Klotzbach et al. 2019). Here we found that the occurrence of standing MJO coincides with significant westerly QBO phases (WQBO) (Fig. 8e), in agreement with the conclusion that there is more MC barrier effect during WQBO than ~~EQBO~~ (Zhang and Zhang 2018). The occurrence of slow-propagating MJO is related to significant ~~easterly QBO phases (EQBO)~~ (Fig. 8g). However, there is no significant relationship between the QBO and the other two clusters of MJO (this conclusion is valid even for December–February when the QBO–MJO connection is most robust) (Figs. 8f,h).

The model accurately predicts the corresponding interannual variability associated with ENSO and QBO (Fig. ES6). Similar to the literature (Lim et al. 2019; Marshall et al. 2017), the impacts of QBO on the MJO prediction skill is clearly shown with a higher prediction skill during EQBO than WQBO (31 vs 27 days) (Fig. ES7). This is also consistent with the finding that the model has better prediction skills for the slow-propagating MJO than the standing MJO (Fig. 4a). Regarding the physical mechanisms to explain the role of QBO on MJO, several possible mechanisms have been proposed including the upper-tropospheric stability, cloud radiative feedbacks, QBO wind anomalies, and the changes to wave propagation (Martin et al. 2021; Yoo and Son 2016; Zhang and Zhang 2018). However, they remain largely untested and there is no consensus on a particular mechanism that can explain all the observed QBO–MJO connections. About how QBO modulates these four types of MJO is an open question. Given the limited sample size of MJO cases (Table 1), the robustness needs to be confirmed by considering more MJO cases.

Predicting the initial development and identifying the precursors

This section focuses on understanding the predictability of the initial development in the Indian Ocean and identifying its potential precursors. First, we assessed the model's skill in predicting the target peak phase of MJO (around day 0) with different lead times (Fig. 9). For the standing MJO, the anomalous enhanced convection in the Indian Ocean is highly predictable even with a 20-day lead time. For the jumping MJO, the predicted active convection in the eastern Indian Ocean is weak and less robust for a 20-day lead forecast. The prediction of the second convection center in the western Pacific is even more challenging, and both the 15- and 20-day lead forecasts fail to capture it. For both the slow and fast-propagating MJO, the drying anomalies in the western Pacific are less predictable than the wetting anomalies in the Indian Ocean. One issue for the slow-propagating MJO is that the westerly wind anomalies to the west of the convection center are substantially underpredicted. This may contribute to the slowdown of its eastward propagation because of the associated underestimated zonal moisture advection. Note that the selected cases are not completely the same at different lead times given the data availability from model hindcasts.

Why does the model have the ability in predicting the initial development of diversified MJO? What are the precursory signals for these four types of MJO? We further examine the time evolution of preceding convection and circulation anomalies from observations (Fig. 10). As a common precursor for all types of MJO, the prevailing easterly wind anomalies in the Indian
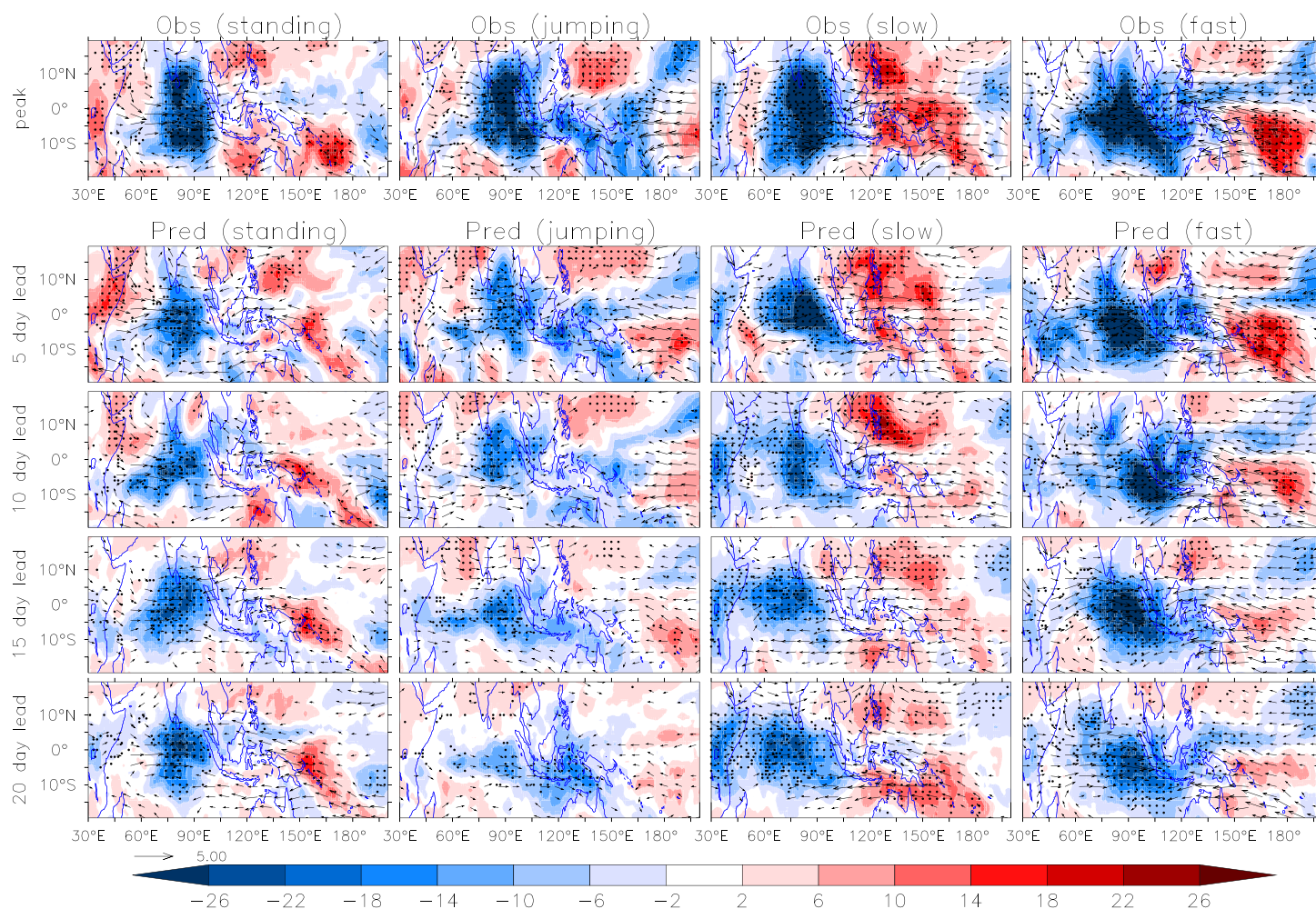
Fig. 9. Model's skill in predicting the target peak phase in the equatorial Indian Ocean (at around day 0) with different lead times for the four types of MJO. The first row shows the observed composite anomalies of OLR (shading; W m⁻²) and 850 hPa winds (m s⁻¹; not shown when wind speed is less than 0.5 m s⁻¹) averaged over days 1–5 for the four MJO clusters. The second to fifth rows are the composite results from model predictions with a lead time of 5 to 20 days, respectively. The black stippling denotes the regions at the 10% significance level for composite OLR anomalies.

Ocean drive the coupled system more subtly toward a state in which the anomalous convection is favored in the Indian Ocean (Fig. 10). The convection anomalies exhibit distinctive precursory conditions that may distinguish the occurrence of different types of MJO. For the standing MJO, pronounced drying anomalies cover nearly the whole tropical Indian Ocean between day −20 and day −10 (Fig. 10, green boxes in the first column), which decay rapidly from day −15 to day −10 before the onset of the wet phase at around day −10. This indicates that the wet phase is preceded by a local dry phase as an oscillatory mode. For the jumping MJO, relatively small-scale convection anomalies are detected in the southern central equatorial Indian Ocean (Fig. 10, green boxes in the second column), and the resultant easterly winds anomalies are responsible for the onset of the wet phase of MJO in the southwest Indian Ocean.

The slow-propagating MJO displays a significant dry phase in the central-to-eastern Indian Ocean during the period between day −20 and day −10 (Fig. 10, green boxes in the third column), which exhibits a clear eastward propagation across the MC to the western Pacific. Note that the dry phase does not show the southward detouring feature near the MC distinguished from its wet phase. For the fast-propagating MJO, the major loading of suppressed convection is anchored in the MC and western Pacific (Fig. 10, green boxes in the fourth column) without an apparent propagation before the initial development of the wet phase in the Indian Ocean. Given the distinctive time evolution of the convection anomalies (Fig. 10), it is inferred that
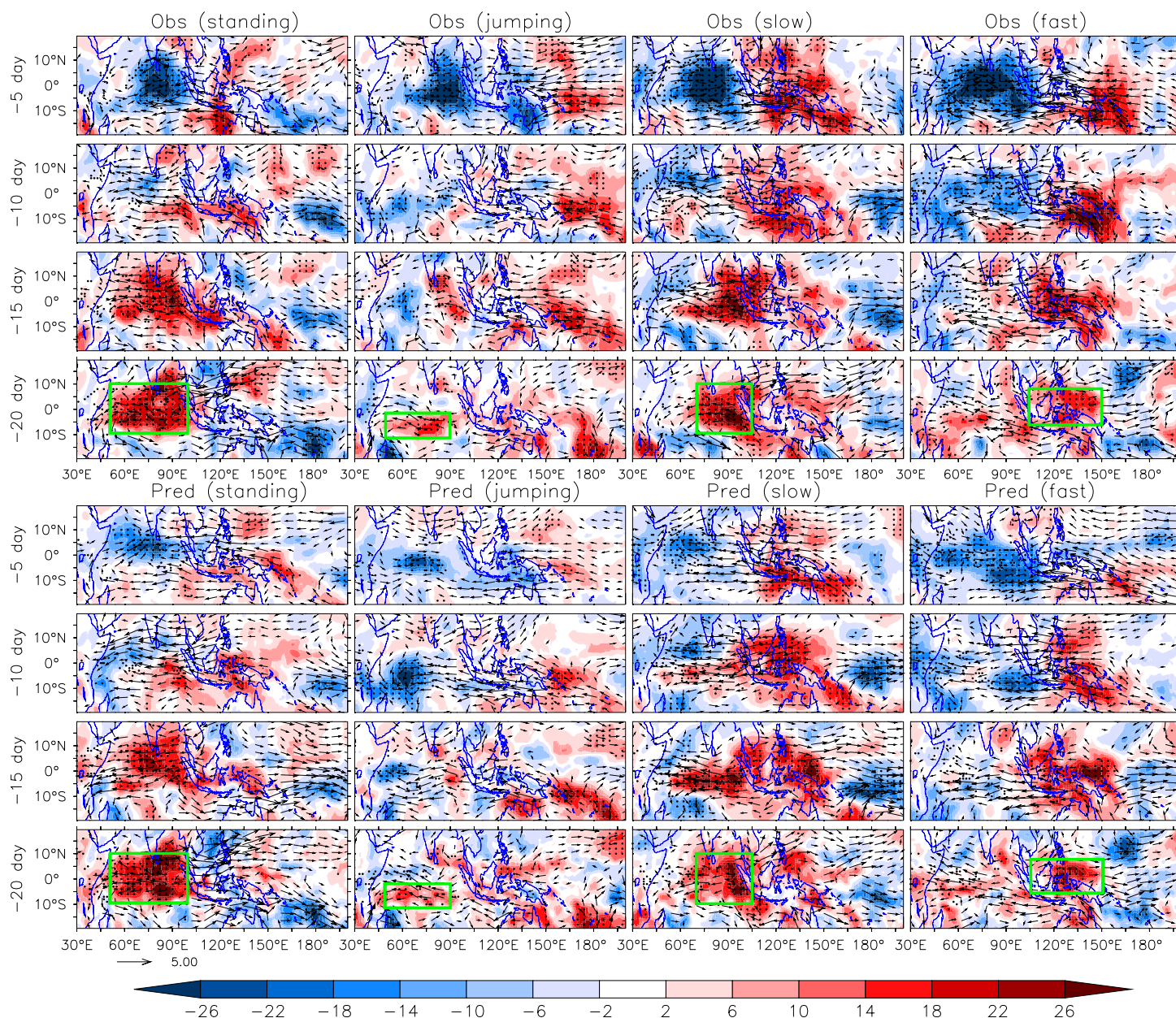
Fig. 10. Observed precursors for the four types of MJO. The first row shows the observed composite anomalies of OLR (shading; W m⁻²) and 850-hPa winds (m s⁻¹; not shown when wind speed is less than 0.5 m s⁻¹) averaged over the period between day −5 and day −1 for four MJO clusters. The second to fourth rows are similar but for 10, 15, and 20 days before the peak phase. The bottom four rows are similar but for the time evolutions of forecast initiated at day −20. The black stippling denotes the regions at the 10% significance level for composite OLR anomalies. Green boxes in the lowest panels for both observations and model forecast denote the key regions with precursory OLR signals.

the standing and slow-propagating MJO are mostly "successive MJO," while the jumping and fast-propagating MJO are mainly "primary MJO." Here the successive MJO is referring to the cases with a preceding event and the primary MJO represents the cases originating from the Indian Ocean (Matthews 2008). The model generally predicts a similar time evolution of convection and circulation anomalies as observations for all types of MJO when initiated at day −20 (Fig. 10).

Prediction of teleconnections

The impacts of the MJO are not just within the tropics but also in the extratropics as well. The MJO's extratropical circulation signature has been studied extensively, and many efforts have been made to unravel the physical processes that underlie the establishment of

the teleconnections forced by MJO (Ferranti et al. 1990; Stan et al. 2017; Tseng et al. 2019). However, many current climate models still have difficulty in realistically simulating MJO, and the error in the Pacific subtropical jet greatly limits the ability to faithfully produce the MJO teleconnection patterns (Henderson et al. 2017; Wang et al. 2020). A skillful prediction of the relevant tropical convection could allow the prediction of its remote teleconnections to become possible.

Chen (2021) has examined the observational circulation anomalies associated with these four types of MJO. Here one example is shown to illustrate the observed and predicted distinctive t2m and 500-hPa geopotential height anomalies (averaged 11–20 days after day 0) associated with these four types of MJO by focusing on the Pacific–North America sector (Fig. 11). For the standing MJO, robust cold t2m anomalies are observed near the Chukchi Sea, northern Canada, and the adjacent seas (Fig. 11a). The jumping MJO excites a zonal wave train circulation over the northeastern Pacific–North America–North Atlantic sector, with a coherent zonal dipole pattern of t2m anomalies in North America and a significant warming over the Greenland Sea and Norwegian Sea regions (Fig. 11b). The slow- and fast-propagating MJO have a similar teleconnection pathway in the Pacific–North America sector, reminiscent of a typical pattern of the North Pacific Oscillation (NPO) mode with a low pressure system over Alaska and the Bering Sea and high pressure in northern North America (Rogers 1981). Compared to the slow-propagating MJO, the fast-propagating MJO induces a slightly southward shifted warming in North America (Fig. 11d vs Fig. 11c). For the fast-propagating MJO, the circulation and surface temperature anomalies in the North Atlantic sector project onto the positive phase of North Atlantic Oscillation (NAO) (Fig. 11d), as documented in many previous studies (Cassou 2008; Lin et al. 2009). It is of interest to note that the teleconnections associated with the standing and propagating MJO resemble very similar patterns with two leading EOF modes of the wintertime cold extremes in North America (Xiang et al. 2020). This implies that the MJO is one of the major drivers and also a key predictability source for the wintertime extremes in North America but that the occurrence of such extremes may be sensitive to the MJO type.

The remarkable teleconnection differences highlight the importance of accurately predicting the propagation characteristic of MJO in the tropics. Inspection of the model hindcasts initiated at around day 0 (strongest convection in the Indian Ocean) reveals a considerable skill in predicting the distinguished circulation and temperature anomalies for the standing, jumping, and fast-propagating MJO (Fig. 11). However, the model struggles to predict the teleconnections associated with the slow-propagating MJO (Fig. 11g). The corresponding pattern correlations between the observed and predicted t2m anomalies are 0.57 (standing), 0.64 (jumping), 0.19 (slow-propagating), and 0.55 (fast-propagating), respectively. We also examined the same time period as in Fig. 11 but initiated at day −5 and found that the model has some skill in predicting the associated teleconnections for the standing and fast-propagating MJO, while the model is limited in its ability to predict the teleconnections for both the jumping and slow-propagating MJO (not shown). The detailed processes leading to the limited skill in predicting its teleconnection remain elusive and require further investigation.

Summary and discussion
Conclusions. Improvements in MJO prediction skills are critical for developing prediction products for various weather and climate phenomena. This study introduces a newly developed S2S prediction system using the GFDL SPEAR global coupled model. The wintertime (November–April) MJO prediction is evaluated using 20-yr hindcasts (2000–19). Results show that the model skillfully predicts the MJO for 30 days before the bivariate ACC of the RMM index drops to 0.5 (Fig. 1). The MJO prediction skill is dependent on the MJO propagation features (Fig. 4).
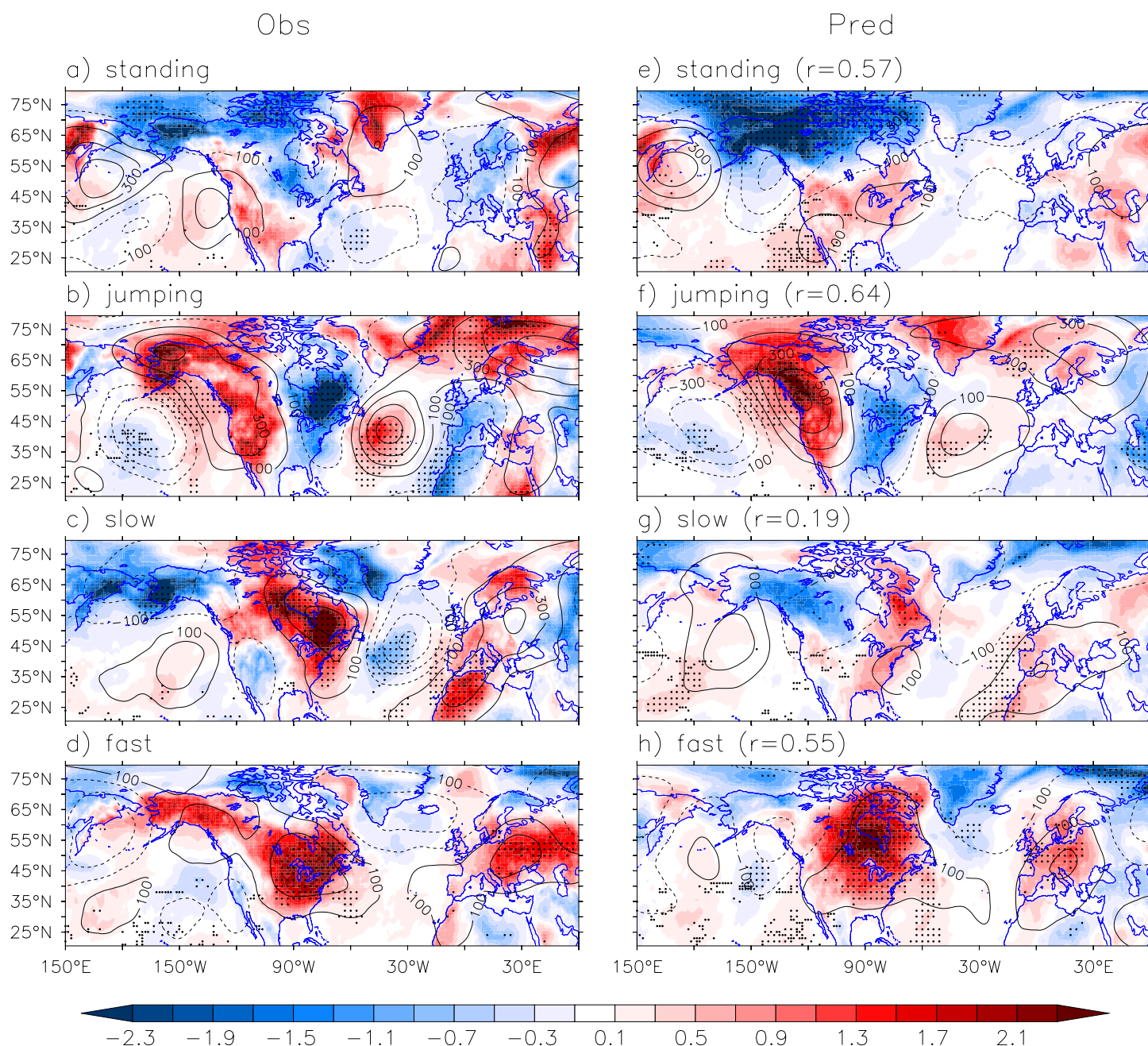
Fig. 11. Observed and predicted teleconnection patterns associated with the four types of MJO. (a)–(d) The composite observational anomalies of 2-m temperature (shading; °C) and 500-hPa geopotential height (contours; m² s⁻²) averaged over 11–20 days after the peak phase (between day 11 and 20) for the four types of MJO. (e)–(h) As in (a)–(d), but for model predictions initiated at peak phase (around day 0). The correlation skills of 2-m temperature anomalies are shown in parentheses in (e)–(h).

The fast-propagating MJO has the best skill of 38 days, followed by the slow-propagating MJO and jumping MJO (31 days), and then the standing MJO (23 days). The diversified skills for different types of MJO are related to their contrasting skills ~~initiated at~~ weak MJO and their amplitude difference (Fig. 5). To further improve the MJO prediction in SPEAR, the key is to advance the prediction of standing MJO given its large gap with its potential predictability ~~(15 days)~~ (Fig. 4). The slow-propagating MJO detours southward when traversing the MC and suffers the MC prediction barrier ~~effect~~, while the fast-propagating MJO propagates across the central MC without the MC prediction barrier issue (Figs. 6 and 7). The intensity of Kelvin waves and the zonal spatial scales, potentially modulated by the background interannual variability, are essential in determining their different propagations (Figs. 7 and 8). The MJO

diversity is modulated by interannual variabilities from ENSO and QBO. In particular, we found that the occurrence of the standing MJO coincides with significant WQBO phases and the slow-propagating MJO is corresponding to significant EQBO phases. The modulation of QBO on MJO diversity partially explains the contrasting MJO prediction skill between two QBO phases.

The SPEAR model exhibits its capability not only in predicting the diversified MJO propagation (Figs. 6 and 7) but also in predicting its initial development in the Indian Ocean (Fig. 9) accompanying by contrasting precursory convection signals (Fig. 10). Distinct teleconnections in the northern extratropics are revealed for these four types of MJO, and the SPEAR model realistically predicts its extratropical teleconnection for the standing, jumping, and fast-propagating MJO (averaged 11–20 days after day 0) (Fig. 11). However, the model has little skill in predicting its observed teleconnections for the slow-propagating MJO despite a useful MJO prediction skill of 31 days. It highlights the complexities and challenges of applying a skillful MJO prediction to the operational prediction of MJO impacts, such as the meteorological variables—t2m and precipitation.

Discussion. Why do the slow-propagating and fast-propagating MJO differ in their propagation pathway when crossing the MC: one through the southern MC and the other through the central MC (Fig. 7)? There are two possible reasons for this. First, for the fast-propagating MJO, the suppressed interannual convective variability to the south of MC may prohibit its southward pathway when crossing the MC (Fig. 8d), resulting in a rather equatorially symmetric propagation over the central MC (Fig. 7). Second, the propagation pathway can be modulated by the seasonal variation of the background mean state. Kim et al. (2017) found that the MJO preferentially detours southward near the MC during December–February (DJF), predominantly related to the meridional mean moisture gradient. Here we reveal the seasonal preference about the occurrence frequency of different types of MJO. There are more slow-propagating cases in DJF than March–April (MA) (9 vs 3), but fewer fast-propagating MJO cases in DJF than MA (4 vs 7) (Table 1), consistent with (Chen 2021). It also implies the MJO propagation speed may have seasonal dependence with fast (slow) propagation speed in DJF (MA). Meanwhile, there are fewer standing MJO cases in MA than DJF (Table 1). The seasonal preference indicates that the background mean state in MA tends to be more favorable for its eastward propagation of MJO than in DJF. Compared to the fast-propagating MJO, the more severe MC prediction barrier problem for the slow-propagating MJO is possibly linked to a more severe mean state bias in DJF than MA. Identifying the potential role and processes of seasonality in regulating the MJO diversity calls for deliberation. There are several other issues that are not addressed here. For example, why does the QBO have pronounced influences on the standing and slow-propagating MJO but not on the other two types of MJO (the seasonal preference of the occurrence of different MJO types may partially explain this as the connection between QBO and MJO is most prominent in DJF)? Why does the model have difficulty in predicting the teleconnections associated with the slow-propagating MJO? Whether and to what extent these findings can be applied to other dynamical models is another issue calling for further studies.

Though the SPEAR model produces a comparable or even better MJO prediction skill than the majority of current operational S2S prediction models (Kim et al. 2018; Vitart 2017), there are also some caveats and limitations for the current configuration, developed for high performance computing constraints. For example, the model has a relatively coarse vertical resolution (33 levels) with a low top atmosphere. The initialization is relatively simple, and the land is not explicitly initialized, although it can be constrained by the atmospheric nudging. The system also suffers the underdispersive issue (the ensemble spread is much smaller than the RMSE) common to many models. These caveats, however, may provide an opportunity to

identify the roles of a better representation of the stratosphere and a sophisticated initialization in S2S prediction and should be explored.

Understanding and isolating skills with a global model are critical for further model development. We hope that this work provides a framework to identify potential issues for MJO prediction in individual models by examining diversified MJO, which may provide guidance for further model development. Given the different impacts from these four types of MJO, operational forecasters may need to consider more than just the RMM index when monitoring the MJO and forecasting its impacts.

The SPEAR seasonal prediction system (Delworth et al. 2020; Lu et al. 2020) is operationally participating in the North American Multi-Model Ensemble (NMME) (Kirtman et al. 2014), but was first developed for research. By developing SPEAR for S2S prediction, we have created a new system for shorter-range prediction that could similarly be used in research to further development in operational modeling. Importantly, the SPEAR model shares two key model components with the Unified Forecast System (UFS) model: the Finite-Volume Cubed-Sphere (FV3) dynamical core (Lin 2004) and MOM6 ocean model (Adcroft et al. 2019). Thus, knowledge derived from the development and use of SPEAR can be used to assist in the development and application of the UFS model.

References

Adames, Á. F., and D. Kim, 2016: The MJO as a dispersive, convectively coupled moisture wave: Theory and observations. *J. Atmos. Sci.*, **73**, 913–941, https://doi.org/10.1175/JAS-D-15-0170.1.

Adcroft, A., and Coauthors, 2019: The GFDL global ocean and sea ice model OM4.0: Model description and simulation features. *J. Adv. Model. Earth Syst.*, **11**, 3167–3211, https://doi.org/10.1029/2019MS001726.

Benedict, J. J., and D. A. Randall, 2007: Observed characteristics of the MJO relative to maximum rainfall. *J. Atmos. Sci.*, **64**, 2332–2354, https://doi.org/10.1175/JAS3968.1.

Bladé, I., and D. L. Hartmann, 1993: Tropical intraseasonal oscillations in a simple nonlinear model. *J. Atmos. Sci.*, **50**, 2922–2939, https://doi.org/10.1175/1520-0469(1993)050<2922:TIOIAS>2.0.CO;2.

Bushuk, M., and Coauthors, 2021: Seasonal prediction and predictability of regional Antarctic sea ice. *J. Climate*, **34**, 6207–6233, https://doi.org/10.1175/JCLI-D-20-0965.1.

C3S, 2017: ERA5: Fifth generation of ECMWF atmospheric reanalyses of the global climate. Copernicus Climate Change Service Climate Data Store, https://cds.climate.copernicus.eu/cdsapp#!/home.

Cassou, C., 2008: Intraseasonal interaction between the Madden–Julian Oscillation and the North Atlantic Oscillation. *Nature*, **455**, 523–527, https://doi.org/10.1038/nature07286.

Chen, G., 2021: Diversity of the global teleconnections associated with the Madden–Julian oscillation. *J. Climate*, **34**, 397–414, https://doi.org/10.1175/JCLI-D-20-0357.1.

——, and B. Wang, 2020: Circulation factors determining the propagation speed of the Madden–Julian oscillation. *J. Climate*, **33**, 3367–3380, https://doi.org/10.1175/JCLI-D-19-0661.1.

DeFlorio, M. J., D. E. Waliser, B. Guan, D. A. Lavers, F. M. Ralph, and F. Vitart, 2018: Global assessment of atmospheric river prediction skill. *J. Hydrometeor.*, **19**, 409–426, https://doi.org/10.1175/JHM-D-17-0135.1.

Delworth, T. L., and Coauthors, 2020: SPEAR: The next generation GFDL modeling system for seasonal to multidecadal prediction and projection. *J. Adv. Model. Earth Syst.*, **12**, e2019MS001895, https://doi.org/10.1029/2019MS001895.

Dong, W., M. Zhao, Y. Ming, and V. Ramaswamy, 2021: Representation of tropical mesoscale convective systems in a general circulation model: Climatology and response to global warming. *J. Climate*, **34**, 5657–5671, https://doi.org/10.1175/JCLI-D-20-0535.1.

Ferranti, L., T. N. Palmer, F. Molteni, and E. Klinker, 1990: Tropical-extratropical interaction associated with the 30–60 day oscillation and its impact on medium and extended range prediction. *J. Atmos. Sci.*, **47**, 2177–2199, https://doi.org/10.1175/1520-0469(1990)047<2177:TEIAWT>2.0.CO;2.

Fu, X., J.-Y. Lee, P.-C. Hsu, H. Taniguchi, B. Wang, W. Wang, and S. Weaver, 2013: Multi-model MJO forecasting during DYNAMO/CINDY period. *Climate Dyn.*, **41**, 1067–1081, https://doi.org/10.1007/s00382-013-1859-9.

Gelaro, R., and Coauthors, 2017: The Modern-Era Retrospective Analysis for Research and Applications, version 2 (MERRA-2). *J. Climate*, **30**, 5419–5454, https://doi.org/10.1175/JCLI-D-16-0758.1.

Haertel, P., 2021: Kelvin/Rossby wave partition of Madden-Julian oscillation circulations. *Climate*, **9**, 2, https://doi.org/10.3390/cli9010002.

Harris, L., and Coauthors, 2020: GFDL SHiELD: A unified system for weather-to-seasonal prediction. *J. Adv. Model. Earth Syst.*, **12**, e2020MS002223, https://doi.org/10.1029/2020MS002223.

Held, I. M., and Coauthors, 2019: Structure and performance of GFDL's CM4.0 climate model. *J. Adv. Model. Earth Syst.*, **11**, 3691–3727, https://doi.org/10.1029/2019MS001829.

Henderson, S. A., E. D. Maloney, and S.-W. Son, 2017: Madden–Julian oscillation Pacific teleconnections: The impact of the basic state and MJO representation in general circulation models. *J. Climate*, **30**, 4567–4587, https://doi.org/10.1175/JCLI-D-16-0789.1.

Hsu, P., and T. Li, 2012: Role of the boundary layer moisture asymmetry in causing the eastward propagation of the Madden–Julian oscillation. *J. Climate*, **25**, 4914–4931, https://doi.org/10.1175/JCLI-D-11-00310.1.

Jiang, X., B. Xiang, M. Zhao, T. Li, S.-J. Lin, Z. Wang, and J.-H. Chen, 2018: Intraseasonal tropical cyclogenesis prediction in a global coupled model system. *J. Climate*, **31**, 6209–6227, https://doi.org/10.1175/JCLI-D-17-0454.1.

——, and Coauthors, 2020: Fifty years of research on the Madden-Julian oscillation: Recent progress, challenges, and perspectives. *J. Geophys. Res. Atmos.*, **125**, e2019JD030911, https://doi.org/10.1029/2019JD030911.

Kaufman, L., and P. J. Rousseeuw, 2009: *Finding Groups in Data: An Introduction to Cluster Analysis*. John Wiley & Sons, 342 pp.

Kerns, B. W., and S. S. Chen, 2020: A 20-year climatology of Madden-Julian oscillation convection: Large-scale precipitation tracking from TRMM-GPM rainfall. *J. Geophys. Res. Atmos.*, **125**, e2019JD032142, https://doi.org/10.1029/2019JD032142.

Kiladis, G. N., K. H. Straub, and P. T. Haertel, 2005: Zonal and vertical structure of the Madden–Julian oscillation. *J. Atmos. Sci.*, **62**, 2790–2809, https://doi.org/10.1175/JAS3520.1.

Kim, D., J.-S. Kug, and A. H. Sobel, 2014: Propagating versus nonpropagating Madden–Julian oscillation events. *J. Climate*, **27**, 111–125, https://doi.org/10.1175/JCLI-D-13-00084.1.

——, H. Kim, and M.-I. Lee, 2017: Why does the MJO detour the Maritime Continent during austral summer? *Geophys. Res. Lett.*, **44**, 2579–2587, https://doi.org/10.1002/2017GL072643.

Kim, H., F. Vitart, and D. E. Waliser, 2018: Prediction of the Madden–Julian oscillation: A review. *J. Climate*, **31**, 9425–9443, https://doi.org/10.1175/JCLI-D-18-0210.1.

——, M. A. Janiga, and K. Pegion, 2019: MJO propagation processes and mean biases in the SubX and S2S reforecasts. *J. Geophys. Res. Atmos.*, **124**, 9314–9331, https://doi.org/10.1029/2019JD031139.

Kirtman, B. P., and Coauthors, 2014: The North American Multimodel Ensemble: Phase-1 seasonal-to-interannual prediction; phase-2 toward developing intraseasonal prediction. *Bull. Amer. Meteor. Soc.*, **95**, 585–601, https://doi.org/10.1175/BAMS-D-12-00050.1.

Klotzbach, P., S. Abhik, H. H. Hendon, M. Bell, C. Lucas, A. G. Marshall, and E. C. J. Oliver, 2019: On the emerging relationship between the stratospheric quasi-biennial oscillation and the Madden-Julian oscillation. *Sci. Rep.*, **9**, 2981, https://doi.org/10.1038/s41598-019-40034-6.

Lee, C.-Y., S. J. Camargo, F. Vitart, A. H. Sobel, and M. K. Tippett, 2018: Subseasonal tropical cyclone genesis prediction and MJO in the S2S dataset. *Wea. Forecasting*, **33**, 967–988, https://doi.org/10.1175/WAF-D-17-0165.1.

——, and Coauthors, 2020: Subseasonal predictions of tropical cyclone occurrence and ACE in the S2S dataset. *Wea. Forecasting*, **35**, 921–938, https://doi.org/10.1175/WAF-D-19-0217.1.

Li, T., L. Wang, M. Peng, B. Wang, C. Zhang, W. Lau, and H.-C. Kuo, 2018: A paper on the tropical intraseasonal oscillation published in 1963 in a Chinese journal. *Bull. Amer. Meteor. Soc.*, **99**, 1765–1779, https://doi.org/10.1175/BAMS-D-17-0216.1.

Liebmann, B., and C. A. Smith, 1996: Description of a complete (interpolated) outgoing longwave radiation dataset. *Bull. Amer. Meteor. Soc.*, **77**, 1275–1277, https://doi.org/10.1175/1520-0477-77.6.1274.

Lim, Y., S.-W. Son, and D. Kim, 2018: MJO prediction skill of the subseasonal-to-seasonal prediction models. *J. Climate*, **31**, 4075–4094, https://doi.org/10.1175/JCLI-D-17-0545.1.

——, ——, A. G. Marshall, H. H. Hendon, and K.-H. Seo, 2019: Influence of the QBO on MJO prediction skill in the subseasonal-to-seasonal prediction models. *Climate Dyn.*, **53**, 1681–1695, https://doi.org/10.1007/s00382-019-04719-y.

Lin, H., G. Brunet, and J. Derome, 2008: Forecast skill of the Madden–Julian oscillation in two Canadian atmospheric models. *Mon. Wea. Rev.*, **136**, 4130–4149, https://doi.org/10.1175/2008MWR2459.1.

——, ——, and ——, 2009: An observed connection between the North Atlantic oscillation and the Madden–Julian oscillation. *J. Climate*, **22**, 364–380, https://doi.org/10.1175/2008JCLI2515.1.

——, ——, and S. Fontecilla Juan, 2010: Impact of the Madden-Julian Oscillation on the intraseasonal forecast skill of the North Atlantic Oscillation. *Geophys. Res. Lett.*, **37**, L19803, https://doi.org/10.1029/2010GL044315.

Lin, S.-J., 2004: A "vertically Lagrangian" finite-volume dynamical core for global models. *Mon. Wea. Rev.*, **132**, 2293–2307, https://doi.org/10.1175/1520-0493(2004)132<2293:AVLFDC>2.0.CO;2.

Liu, C., B. Tian, K.-F. Li, G. L. Manney, N. J. Livesey, Y. L. Yung, and D. E. Waliser, 2014: Northern Hemisphere mid-winter vortex-displacement and vortex-split stratospheric sudden warmings: Influence of the Madden-Julian Oscillation and Quasi-Biennial Oscillation. *J. Geophys. Res. Atmos.*, **119**, 12 599–12 620, https://doi.org/10.1002/2014JD021876.

Liu, J., Y. Da, T. Li, and F. Hu, 2020: Impact of ENSO on MJO pattern evolution over the maritime continent. *J. Meteor. Res.*, **34**, 1151–1166, https://doi.org/10.1007/s13351-020-0046-2.

Lu, F., and Coauthors, 2020: GFDL's SPEAR seasonal prediction system: initialization and ocean tendency adjustment (OTA) for coupled model predictions. *J. Adv. Model. Earth Syst.*, **12**, e2020MS002149, https://doi.org/10.1029/2020MS002149.

Lyu, M., X. Jiang, Z. Wu, D. Kim, and Á. F. Adames, 2021: Zonal-scale of the Madden-Julian Oscillation and its propagation speed on the interannual time-scale. *Geophys. Res. Lett.*, **48**, e2020GL091239, https://doi.org/10.1029/2020GL091239.

Madden, R. A., and P. R. Julian, 1971: Detection of a 40–50 day oscillation in the zonal wind in the tropical Pacific. *J. Atmos. Sci.*, **28**, 702–708, https://doi.org/10.1175/1520-0469(1971)028<0702:DOADOI>2.0.CO;2.

——, and ——, 1972: Description of global-scale circulation cells in the tropics with a 40–50 day period. *J. Atmos. Sci.*, **29**, 1109–1123, https://doi.org/10.1175/1520-0469(1972)029<1109:DOGSCC>2.0.CO;2.

Marshall, A. G., H. H. Hendon, S.-W. Son, and Y. Lim, 2017: Impact of the quasi-biennial oscillation on predictability of the Madden–Julian oscillation. *Climate Dyn.*, **49**, 1365–1377, https://doi.org/10.1007/s00382-016-3392-0.

Martin, Z., and Coauthors, 2021: The influence of the quasi-biennial oscillation on the Madden–Julian oscillation. *Nat. Rev. Earth Environ.*, **2**, 477–489, https://doi.org/10.1038/s43017-021-00173-9.

Matthews, A. J., 2008: Primary and successive events in the Madden–Julian Oscillation. *Quart. J. Roy. Meteor. Soc.*, **134**, 439–453, https://doi.org/10.1002/qj.224.

Mundhenk, B. D., E. A. Barnes, E. D. Maloney, and C. F. Baggett, 2018: Skillful empirical subseasonal prediction of landfalling atmospheric river activity using the Madden–Julian oscillation and quasi-biennial oscillation. *npj Climate Atmos. Sci.*, **1**, 20177, https://doi.org/10.1038/s41612-017-0008-2.

Murakami, H., T. L. Delworth, W. F. Cooke, M. Zhao, B. Xiang, and P.-C. Hsu, 2020: Detected climatic change in global distribution of tropical cyclones. *Proc. Natl. Acad. Sci. USA*, **117**, 10 706–10 714, https://doi.org/10.1073/pnas.1922500117.

Nardi, K. M., C. F. Baggett, E. A. Barnes, E. D. Maloney, D. S. Harnos, and L. M. Ciasto, 2020: Skillful all-season S2S prediction of U.S. precipitation using the MJO and QBO. *Wea. Forecasting*, **35**, 2179–2198, https://doi.org/10.1175/WAF-D-19-0232.1.

Neena, J. M., J. Y. Lee, D. Waliser, B. Wang, and X. Jiang, 2014: Predictability of the Madden–Julian oscillation in the Intraseasonal Variability Hindcast Experiment (ISVHE). *J. Climate*, **27**, 4531–4543, https://doi.org/10.1175/JCLI-D-13-00624.1.

Rashid, H. A., H. H. Hendon, M. C. Wheeler, and O. Alves, 2011: Prediction of the Madden–Julian oscillation with the POAMA dynamical prediction system. *Climate Dyn.*, **36**, 649–661, https://doi.org/10.1007/s00382-010-0754-x.

Ren, H.-L., J. Wu, C.-B. Zhao, Y.-J. Cheng, and X.-W. Liu, 2016: MJO ensemble prediction in BCC-CSM1.1(m) using different initialization schemes. *Atmos. Ocean. Sci. Lett.*, **9**, 60–65, https://doi.org/10.1080/16742834.2015.1116217.

Reynolds, R. W., T. M. Smith, C. Liu, D. B. Chelton, K. S. Casey, and M. G. Schlax, 2007: Daily high-resolution-blended analyses for sea surface temperature. *J. Climate*, **20**, 5473–5496, https://doi.org/10.1175/2007JCLI1824.1.

Rogers, J. C., 1981: The North Pacific Oscillation. *J. Climatol.*, **1**, 39–57, https://doi.org/10.1002/joc.3370010106.

Stan, C., D. M. Straus, J. S. Frederiksen, H. Lin, E. D. Maloney, and C. Schumacher, 2017: Review of tropical-extratropical teleconnections on intraseasonal time scales. *Rev. Geophys.*, **55**, 902–937, https://doi.org/10.1002/2016RG000538.

Tseng, K.-C., E. Maloney, and E. Barnes, 2019: The consistency of MJO teleconnection patterns: An explanation using linear Rossby wave theory. *J. Climate*, **32**, 531–548, https://doi.org/10.1175/JCLI-D-18-0211.1.

Vitart, F., 2009: Impact of the Madden Julian Oscillation on tropical storms and risk of landfall in the ECMWF forecast system. *Geophys. Res. Lett.*, **36**, L15802, https://doi.org/10.1029/2009GL039089.

——, 2017: Madden–Julian Oscillation prediction and teleconnections in the S2S database. *Quart. J. Roy. Meteor. Soc.*, **143**, 2210–2220, https://doi.org/10.1002/qj.3079.

Wang, B., 1988: Dynamics of tropical low-frequency waves: An analysis of the moist Kelvin wave. *J. Atmos. Sci.*, **45**, 2051–2065, https://doi.org/10.1175/1520-0469(1988)045<2051:DOTLFW>2.0.CO;2.

——, and H. Rui, 1990: Synoptic climatology of transient tropical intraseasonal convection anomalies: 1975–1985. *Meteor. Atmos. Phys.*, **44**, 43–61, https://doi.org/10.1007/BF01026810.

——, and S.-S. Lee, 2017: MJO propagation shaped by zonal asymmetric structures: Results from 24 GCM simulations. *J. Climate*, **30**, 7933–7952, https://doi.org/10.1175/JCLI-D-16-0873.1.

——, F. Liu, and G. Chen, 2016: A trio-interaction theory for Madden–Julian oscillation. *Geosci. Lett.*, **3**, 34, https://doi.org/10.1186/s40562-016-0066-z.

——, G. Chen, and F. Liu, 2019: Diversity of the Madden-Julian Oscillation. *Sci. Adv.*, **5**, eaax0220, https://doi.org/10.1126/sciadv.aax0220.

Wang, J., H. Kim, D. Kim, S. A. Henderson, C. Stan, and E. D. Maloney, 2020: MJO teleconnections over the PNA region in climate models. Part II: Impacts of the MJO and basic state. *J. Climate*, **33**, 5081–5101, https://doi.org/10.1175/JCLI-D-19-0865.1.

Wang, S., M. K. Tippett, A. H. Sobel, Z. K. Martin, and F. Vitart, 2019: Impact of the QBO on prediction and predictability of the MJO convection. *J. Geophys. Res. Atmos.*, **124**, 11 766–11 782, https://doi.org/10.1029/2019JD030575.

Weaver, S. J., W. Wang, M. Chen, and A. Kumar, 2011: Representation of MJO variability in the NCEP climate forecast system. *J. Climate*, **24**, 4676–4694, https://doi.org/10.1175/2011JCLI4188.1.

Wei, Y., and H.-L. Ren, 2019: Modulation of ENSO on fast and slow MJO modes during boreal winter. *J. Climate*, **32**, 7483–7506, https://doi.org/10.1175/JCLI-D-19-0013.1.

Wheeler, M. C., and H. H. Hendon, 2004: An all-season real-time multivariate MJO index: Development of an index for monitoring and prediction. *Mon. Wea. Rev.*, **132**, 1917–1932, https://doi.org/10.1175/1520-0493(2004)132<1917:AARMMI>2.0.CO;2.

Wu, J., H.-L. Ren, B. Lu, P. Zhang, C. Zhao, and X. Liu, 2020: Effects of moisture initialization on MJO and its teleconnection prediction in BCC subseasonal coupled model. *J. Geophys. Res. Atmos.*, **125**, e2019JD031537, https://doi.org/10.1029/2019JD031537.

Xiang, B., and Coauthors, 2015a: Beyond weather time-scale prediction for Hurricane Sandy and Super Typhoon Haiyan in a global climate model. *Mon. Wea. Rev.*, **143**, 524–535, https://doi.org/10.1175/MWR-D-14-00227.1.

——, M. Zhao, X. Jiang, S.-J. Lin, T. Li, X. Fu, and G. Vecchi, 2015b: The 3–4-week MJO prediction skill in a GFDL coupled model. *J. Climate*, **28**, 5351–5364, https://doi.org/10.1175/JCLI-D-15-0102.1.

——, Y. Q. Sun, J.-H. Chen, N. C. Johnson, and X. Jiang, 2020: Subseasonal prediction of land cold extremes in boreal wintertime. *J. Geophys. Res. Atmos.*, **125**, e2020JD032670, https://doi.org/10.1029/2020JD032670.

Xie, Y.-B., S.-J. Chen, I.-L. Zhang, and Y.-L. Hung, 1963: A preliminarily statistic and synoptic study about the basic currents over southeastern Asia and the initiation of typhoon (in Chinese). *Acta Meteor. Sin.*, **33**, 206–217.

Yoo, C., and S.-W. Son, 2016: Modulation of the boreal wintertime Madden-Julian oscillation by the stratospheric quasi-biennial oscillation. *Geophys. Res. Lett.*, **43**, 1392–1398, https://doi.org/10.1002/2016GL067762.

Zhang, C., and B. Zhang, 2018: QBO-MJO Connection. *J. Geophys. Res. Atmos.*, **123**, 2957–2967, https://doi.org/10.1002/2017JD028171.

——, Á. F. Adames, B. Khouider, B. Wang, and D. Yang, 2020: Four theories of the Madden-Julian Oscillation. *Rev. Geophys.*, **58**, e2019RG000685, https://doi.org/10.1029/2019RG000685.

Zhao, M., 2020: Simulations of atmospheric rivers, their variability, and response to global warming using GFDL's new high-resolution general circulation model. *J. Climate*, **33**, 10 287–10 303, https://doi.org/10.1175/JCLI-D-20-0241.1.

——, and Coauthors, 2018a: The GFDL global atmosphere and land model AM4.0/LM4.0: 1. Simulation characteristics with prescribed SSTs. *J. Adv. Model. Earth Syst.*, **10**, 691–734, https://doi.org/10.1002/2017MS001208.

——, and Coauthors, 2018b: The GFDL global atmosphere and land model AM4.0/LM4.0: 2. Model description, sensitivity studies, and tuning strategies. *J. Adv. Model. Earth Syst.*, **10**, 735–769, https://doi.org/10.1002/2017MS001209.

Zhu, J., and A. Kumar, 2019: Role of sea surface salinity feedback in MJO predictability: A study with CFSv2. *J. Climate*, **32**, 5745–5759, https://doi.org/10.1175/JCLI-D-18-0755.1.

——, ——, and W. Wang, 2020: Dependence of MJO predictability on convective parameterizations. *J. Climate*, **33**, 4739–4750, https://doi.org/10.1175/JCLI-D-18-0552.1.